Feasibility to probe the dynamical scotogenic model at the LHC

Gustavo Ardila-Tafurth,[*] Andrés Flórez,[†] Cristian Rodríguez,[‡] and Maud Sarazin[§]
Departamento de Física, Universidad de los Andes, Bogotá 111711, Colombia

Óscar Zapata[‖]
Instituto de Física, Universidad de Antioquia, Calle 70 # 52-21, Apartado Aéreo 1226, Medellín, Colombia

(Received 24 December 2025; accepted 13 May 2026; published 5 June 2026)

We perform a feasibility study to probe dark matter (DM) production at the LHC within a global $U(1)_L$ scotogenic model. The study is conducted using the Markov chain Monte Carlo numerical method, considering the viable parameter space of the model allowed by experimental constraints such as neutrino oscillation data, the Higgs to invisible branching fraction, and DM observables. The production of scalar and fermionic DM candidates, predicted by the model, is then studied under the LHC conditions for different luminosity scenarios imposing compressed mass spectra conditions between the lightest fermion and the $\mathbb{Z}_2$ odd scalars. We study two production mechanisms, Drell-Yan and vector boson fusion. We find that the Drell-Yan mechanism gives better detection prospects for fermionic DM masses between 100 and 220 GeV at high-luminosity scenarios.

DOI: 10.1103/f3fq-gbct

I. INTRODUCTION

The Standard Model (SM) of particle physics, formulated in the 1970s, is one of the most precise theoretical frameworks in physics. It describes particle interactions through electromagnetic, weak, and strong forces with precision up to 12 significant figures [1]. The SM employs the principle of gauge invariance to explain fundamental interactions between fermions, which are the elementary building blocks of known matter. These interactions are mediated by gauge bosons and are framed within the $\mathrm{SU}(3)_C \times \mathrm{SU}(2)_L \times \mathrm{U}(1)_Y$ symmetry group. In this model, elementary particles acquire mass through the Higgs mechanism, based on the concept of electroweak symmetry breaking (EWSB) [2–5].

Despite being our most accurate theory to date, there are several theoretical questions and experimental conundrums that the SM does not answer. These include the matter-antimatter asymmetry [6–8], the particle nature of dark matter (DM) [9–11], and the origin of neutrino masses [12,13], among others. These limitations suggest that the SM may be just the low-energy limit of a broader theory. Therefore, a plethora of extended versions of the SM, referred to as Beyond Standard Model (BSM) scenarios, have been proposed to address these current issues.

A particularly compelling hypothesis addressing the particle nature of DM is the weakly interacting massive particle (WIMP) scenario. WIMPs feature masses and interaction strengths at the electroweak scale [14,15], naturally providing the observed relic density through thermal freeze-out [16] in the early Universe. Because of their appealing theoretical properties and testability in direct and indirect detection experiments, WIMPs remain among the most extensively studied DM candidates [17,18].

Regarding the origin of neutrino masses, experimental observations of neutrino oscillations demonstrate the existence of at least two nonzero mass eigenstates, in clear conflict with the SM prediction of massless neutrinos [19,20]. One of the most prominent neutrino mass generation methods is the so-called tree-level seesaw mechanism [21–25]. This type of mechanism provides an elegant explanation for neutrino masses with minimal additions to the SM particle content. However, high-scale seesaw scenarios require either extremely heavy new states or very small Yukawa couplings, placing them beyond the reach of current and near-future experimental tests. To reduce the energy scale of new physics and construct experimentally testable models, several alternative strategies have been proposed, including higher-dimensional neutrino mass operators, small lepton-number-violating interactions, and radiative neutrino mass generation mechanisms via loop processes [26].

[*]Contact author: ga.ardila10@uniandes.edu.co
[†]Contact author: ca.florez@uniandes.edu.co
[‡]Contact author: c.rodrigez45@uniandes.edu.co
[§]Contact author: m.sarazin@uniandes.edu.co
[‖]Contact author: oalberto.zapata@udea.edu.co

Published by the American Physical Society under the terms of the Creative Commons Attribution 4.0 International license. Further distribution of this work must maintain attribution to the author(s) and the published article's title, journal citation, and DOI. Funded by SCOAP³.

Among the models that generate neutrino masses through loop processes, scotogenic models are particularly appealing, as they unify the origin of neutrino masses and DM, treating them not as separate problems but as interconnected pieces of the same puzzle [27,28]. In the simplest scotogenic model [29,30], the SM is extended with a $\mathrm{SU}(2)_L$ doublet, η, and three Majorana-like fermion singlets, N_i. These new particles transform as odd states under a $\mathbb{Z}_2$ symmetry, which stabilizes the DM candidates. This model naturally gives rise to a rich DM phenomenology [30–32] since the DM candidate can be either a scalar or a fermion. Neutrino masses are then generated radiatively at one-loop level, with the new particle content circulating in the loop, leading to collider and lepton-flavor-violating (LFV) signals [33,34]. Beyond the simplest realization, other scotogenic models have been explored in several studies [34–38], and their phenomenological implications have been examined in numerous subsequent works [39–51].

This paper explores an extension of the scotogenic model, referred to as the dynamical scotogenic model [52–54]. The model extends the symmetry group by introducing a global $\mathrm{U}(1)_L$ symmetry, which is then spontaneously broken by the nontrivial vacuum expectation value (VEV) of a singlet scalar field, σ. This breaking induces a mass term for the N_i, thanks to their Yukawa interactions with the σ scalar,[1] and delivers a pseudo-Goldstone boson—the Majoron J—whose interactions with leptons give rise to new LFV processes. Additionally, the presence of new fields leads to novel DM interactions in the early Universe, enriching the phenomenology with respect to the simplest scotogenic model.

The possibility of testing the scotogenic model (as well as some of its extensions) at particle colliders has been proposed in several phenomenological studies [57–61]. However, a detailed study to determine the experimental feasibility of probing the dynamical scotogenic model has not yet been conducted. This work presents a comprehensive phenomenological study of the collider feasibility of the dynamical scotogenic model, building upon preliminary analyses performed in Refs. [52–54]. We investigate the detectability of the DM candidates by considering both Drell-Yan (DY) and vector boson fusion (VBF) production mechanisms at the LHC. Our study first determines the viable parameter space, ensuring compatibility with DM, neutrino oscillation data, LFV processes, and Higgs invisible decay constraints through a Markov chain Monte Carlo (MCMC) analysis. We identify DY processes involving fermionic DM as the most promising detection strategy. Such processes could be probed at the High-Luminosity LHC (HL-LHC) for DM masses in the range of 100 to 220 GeV.

The paper is organized as follows. First, Sec. II introduces the model, including its particle content, interactions, and mass spectrum. In Sec. III, we present the methodological framework used to explore the parameter space of the model, incorporating all relevant experimental constraints to identify the viable regions featuring either a pseudoscalar or a fermionic DM candidate. Section IV is devoted to the analysis of the impact of direct and indirect detection experiments on the allowed parameter space. In this section, we also simulate event generation for LHC conditions, obtaining the corresponding production cross sections as a function of the DM candidate mass. Then, we evaluate the feasibility of probing different benchmark points at the LHC for various luminosity scenarios. Finally, in Sec. V, we summarize our findings and present our conclusions.

II. THE MODEL

The dynamical scotogenic model [52–54] extends the fermion content of the SM by including three additional Majorana fermions (N_i, $i = \{1, 2, 3\}$). The lepton number conservation is ensured by introducing a global $\mathrm{U}(1)_L$ symmetry, which is spontaneously broken by the VEV of a new singlet scalar field σ.

Besides this singlet, a $\mathrm{SU}(2)_L$ scalar doublet field (η) is also included to couple the SM leptons to the Majorana fermions, thus giving rise to nonzero radiative masses for the SM neutrinos. All the N_i and the extra scalar doublet are considered to be odd under an additional $\mathbb{Z}_2$ symmetry, while SM particles and the additional singlet scalar are even. This simple approach stabilizes the lightest Z_2-odd particle of the model, naturally becoming a feasible DM candidate. Depending on the specific realization, the DM particle can be either scalar or fermionic, a distinction that shapes the allowed parameter space. The particle content and symmetries of the model are described in Table I.

The $\mathbb{Z}_2 \times \mathrm{U}(1)_L$ invariant scalar potential is given by

$$\begin{aligned}\mathcal{V} = {} & m_{\mathrm{H}}^2 \mathrm{H}^\dagger \mathrm{H} + m_\eta^2 \eta^\dagger \eta + m_\sigma^2 \sigma^\dagger \sigma + \frac{\lambda_1}{2} (\mathrm{H}^\dagger \mathrm{H})^2 \\ & + \frac{\lambda_2}{2} (\eta^\dagger \eta)^2 + \frac{\lambda_\sigma}{2} (\sigma^\dagger \sigma)^2 + \lambda_3 (\mathrm{H}^\dagger \mathrm{H})(\eta^\dagger \eta) \\ & + \lambda_3^{\mathrm{H}\sigma} (\mathrm{H}^\dagger \mathrm{H})(\sigma^\dagger \sigma) + \lambda_3^{\eta\sigma} (\eta^\dagger \eta)(\sigma^\dagger \sigma) + \lambda_4 (\mathrm{H}^\dagger \eta)(\eta^\dagger \mathrm{H}) \\ & + \frac{\lambda_5}{2} [(\mathrm{H}^\dagger \eta)^2 + (\eta^\dagger \mathrm{H})^2], \end{aligned} \tag{1}$$

where the SM Higgs (H) and η doublets are parametrized as

$$\eta = \begin{pmatrix} \eta^+ \\ \frac{\eta_R + i\eta_I}{\sqrt{2}} \end{pmatrix}, \qquad \mathrm{H} = \begin{pmatrix} \mathrm{H}^+ \\ \frac{S_{\mathrm{H}} + iA_{\mathrm{H}} + v}{\sqrt{2}} \end{pmatrix}, \tag{2}$$

while for the scalar singlet,

$$\sigma = \frac{1}{\sqrt{2}} (S_\sigma + iA_\sigma + v_\sigma). \tag{3}$$

The charge assignment ensures that only the SM leptons, and not quarks, couple to the dark sector. The relevant

[1]Pioneering work in this sector was carried out in [55,56], which is considered an extension of the type I tree-level seesaw mechanism.

TABLE I. Particle contents of the dynamical scotogenic model and their representations under the electroweak gauge groups and global symmetries.

	ℓ_i	e_{Ri}	N_i	H	σ	η
$SU(2)_L$	**2**	**1**	**1**	**2**	**1**	**2**
$U(1)_Y$	$-\frac{1}{2}$	-1	0	$\frac{1}{2}$	0	$\frac{1}{2}$
$U(1)_L$	1	1	1	0	-2	0
$\mathbb{Z}_2$	1	1	-1	1	1	-1

interaction terms in the Lagrangian density for the new fermionic sector are given by

$$\mathcal{L} \supset y_{ij}\overline{\ell_i}\tilde{\eta}N_j + \kappa_{ij}\overline{N_i}^c N_j \sigma + \text{H.c.}; \quad i,j = 1,2,3. \tag{4}$$

In Eq. (4), the term κ is a 3×3 matrix, which, in our study, is considered to be diagonal without loss of generality.

A. Scalar and fermion spectrum at tree level

Because of the $\lambda_3^{H\sigma}$ term in the potential, the CP-even components of the H and the σ scalar fields mix to form two physical eigenstates, h_1 and h_2, defined as

$$\begin{pmatrix} h_1 \\ h_2 \end{pmatrix} = \begin{pmatrix} \cos\alpha & \sin\alpha \\ -\sin\alpha & \cos\alpha \end{pmatrix} \begin{pmatrix} S_H \\ S_\sigma \end{pmatrix}. \tag{5}$$

From this mixing, we identify h_1 as the SM Higgs boson, with an effective mass of $m_{h_1} \approx 125$ GeV [62]. While the alternative identification (in which the heavier state h_2 corresponds to the observed Higgs boson) is possible, this scenario is subject to strong experimental constraints. In particular, the presence of a lighter scalar requires suppressed mixing with the SM Higgs to evade bounds from LEP and LHC searches and may be further constrained by limits on exotic Higgs decays. For these reasons, we focus on the scenario where h_1 is identified with the observed Higgs boson. The possibility of a lighter Higgs-like scalar within scotogenic frameworks has been explored, for instance, in Ref. [63]. From the potential, the tree-level masses of the two physical scalar states are given by[2]

$$m^2_{h_{1,2}} = \frac{\lambda_1}{2}v^2 + \frac{\lambda_\sigma}{2}v_\sigma^2 \mp \frac{1}{2}\Delta, \tag{6}$$

with $\Delta = \sqrt{(2\lambda_3^{H\sigma} v v_\sigma)^2 + (\lambda_1 v^2 - \lambda_\sigma v_\sigma^2)^2}$. The mixing angle α can be found in terms of the couplings via the expression

$$\tan\alpha = \frac{2\lambda_3^{H\sigma} v v_\sigma}{\lambda_1 v^2 - \lambda_\sigma v_\sigma^2 - \Delta}. \tag{7}$$

This expression is relevant for computing the limit on the branching ratio for the Higgs to invisible decays, as outlined in Ref. [64]:

$$\cos(\alpha)^2 \text{BR}(h \to \text{invisible}) < 0.11. \tag{8}$$

Regarding the CP-odd fields, it can be shown that the structure of the potential, together with the $U(1)_L \times \mathbb{Z}_2$ charge assignation, forbids bilinear terms between the A_H and A_σ fields, leading to unmixed massless states. Hence, the field A_H corresponds to the longitudinal component of the SM Z boson, while A_σ is identified as a physical massless Goldstone boson (the Majoron).

Regarding the Z_2-odd scalar fields, there are no mass mixing terms; consequently, their masses are

$$\begin{aligned} m^2_{\eta_R} &= m^2_\eta + \frac{1}{2}\lambda_3^{\eta\sigma} v_\sigma^2 + \frac{1}{2}(\lambda_3 + \lambda_4 + \lambda_5)v^2, \\ m^2_{\eta_I} &= m^2_\eta + \frac{1}{2}\lambda_3^{\eta\sigma} v_\sigma^2 + \frac{1}{2}(\lambda_3 + \lambda_4 - \lambda_5)v^2, \\ m^2_{\eta^\pm} &= m^2_\eta + \frac{1}{2}(\lambda_3 v^2 + \lambda_3^{\eta\sigma} v_\sigma^2). \end{aligned} \tag{9}$$

The extra fermions acquire their masses at tree level via the κ term, with

$$M_{N_\alpha} = \sqrt{2}\kappa_{\alpha\alpha} v_\sigma, \tag{10}$$

where we assume a hierarchical mass spectrum, that is, $M_{N_1} < M_{N_2} < M_{N_3}$.

The DM candidate in this model is identified as the lightest neutral $\mathbb{Z}_2$-odd particle. In principle, three fields may fulfill this role: the Majorana fermion N_1, the CP-even scalar η_R, and the CP-odd scalar η_I. However, for positive values of the λ_5 coupling, a mass splitting arises that renders η_R heavier than η_I, thereby leaving N_1 and η_I as the only viable candidates. In this work, we investigate the phenomenology associated with each of these scenarios.

B. Neutrino masses

Neutrino masses are generated radiatively through the y_{ij} interactions in Eq. (4), as illustrated in Fig. 1. The elements of the 3×3 neutrino mass matrix take the form [30]

$$(M_\nu)_{ij} = \sum_{k=1}^{3} \frac{y_{ik}y_{jk}^*}{32\pi^2} M_{N_k} \left[\frac{m^2_{\eta_R}}{m^2_{\eta_R} - M^2_{N_k}} \ln\left(\frac{m^2_{\eta_R}}{M^2_{N_k}}\right) - \frac{m^2_{\eta_I}}{m^2_{\eta_I} - M^2_{N_k}} \ln\left(\frac{m^2_{\eta_I}}{M^2_{N_k}}\right) \right]. \tag{11}$$

[2]In our study, all analytical and numerical computations, except for the neutrino mass generation, are performed at tree level.

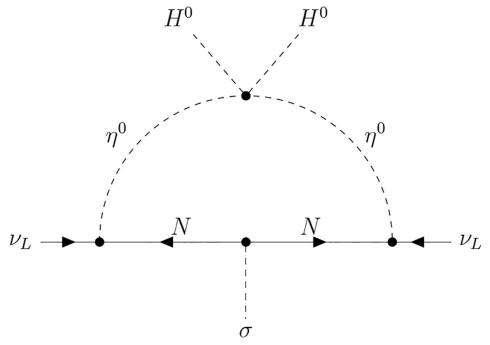


FIG. 1. Representative Feynman diagram illustrating the generation of the neutrino mass matrix element $(M_\nu)_{ij}$ in the physical basis. The η^0 state represents both the neutral scalar η_R and the pseudoscalar η_I, while N denotes any of the three new Majorana fermions running in the loop.

This mechanism naturally accommodates three nonzero neutrino masses. Assuming a normal mass ordering, $m_1 < m_2 < m_3$, the parameter space must be aligned with current experimental observations for the squared mass differences [19,20], Δm^2_{21} and Δm^2_{31}. These stringent requirements, however, place tight constraints on the Yukawa couplings, often making it challenging to identify compatible solutions. To overcome this, we adopt the Casas-Ibarra parametrization [65], where the Yukawa couplings are expressed in terms of masses and neutrino mixing angles as

$$y = \sqrt{\Lambda^{-1}} O \sqrt{\hat{M}_\nu} U^\dagger_{\text{PMNS}}. \tag{12}$$

Here, y is the Yukawa coupling matrix, O is an arbitrary 3×3 orthogonal matrix, U_{PMNS} is the PMNS mixing matrix, and $\Lambda = \text{Diag}(\Lambda_i)$ is a diagonal matrix encoding the loop functions, with

$$\Lambda_i = \frac{M_{N_i}}{32\pi^2}\left[\frac{m^2_{\eta_R}}{m^2_{\eta_R} - M^2_{N_i}} \ln\left(\frac{m^2_{\eta_R}}{M^2_{N_i}}\right) - \frac{m^2_{\eta_I}}{m^2_{\eta_I} - M^2_{N_i}} \ln\left(\frac{m^2_{\eta_I}}{M^2_{N_i}}\right)\right]. \tag{13}$$

III. METHODOLOGICAL SETUP

The first step of our study is to analyze the behavior of the relic abundance of the given DM candidate as a function of its mass. The model is implemented and its particle spectrum is generated using the software SARAH (version 4.15.1) [66–69]; then, the SPHENO package (version 4.0.5) is used [70–72], at leading order, to compute low-energy observables and rates of LFV processes and to estimate the Higgs to invisible branching ratio. The relic abundance, spin-independent DM-nucleon scattering cross section and the average annihilation cross section times velocity for indirect detection are calculated using MICROMEGAS (version 5.3.41) [73]. In this work, the scalar and fermion mass spectrum is computed at tree level, while neutrino masses are evaluated at one loop. We note that one-loop corrections to the scalar masses, as implemented, for instance, in SARAH/SPHENO, can induce shifts of a few GeV in the *CP*-even sector and sub-GeV corrections in the inert scalar mass splittings. Given that our analysis allows for a ± 3 GeV window around the Higgs mass and focuses on compressed spectra with mass splittings of $\mathcal{O}(10)$ GeV, these effects do not qualitatively modify our results [50]. All relevant experimental constraints from Table II are incorporated into our analysis via an MCMC [74] numerical code. Furthermore, using FEYNRULES (version 2.3) [75], we generate a universal Feynman output (UFO) [76] module for MADGRAPH5_aMCNLO (version 3.1.0) [77]. The XSLHA PYTHON package (version 0.2.2) [78] is then used to transfer the SPHENO output into the MadGraph parameter cards, in order to calculate the production cross sections for collider analysis at the LHC.

TABLE II. Experimental constraints applied in the numerical analysis, with the majority provided as upper limits at the 90% confidence level.

Observable	Constraint
m_{h_1}	125.25 ± 3.0 GeV
$\text{BR}(\mu^- \to e^-\gamma)$	$<4.2 \times 10^{-13}$
$\text{BR}(\tau^- \to e^-\gamma)$	$<3.3 \times 10^{-8}$
$\text{BR}(\tau^- \to \mu^-\gamma)$	$<4.2 \times 10^{-8}$
$\text{BR}(\mu^- \to e^-e^+e^-)$	$<1.0 \times 10^{-12}$
$\text{BR}(\tau^- \to e^-e^+e^-)$	$<2.7 \times 10^{-8}$
$\text{BR}(\tau^- \to \mu^-\mu^+\mu^-)$	$<2.1 \times 10^{-8}$
$\text{BR}(\tau^- \to e^-\mu^+\mu^-)$	$<2.7 \times 10^{-8}$
$\text{BR}(\tau^- \to \mu^-e^+e^-)$	$<1.8 \times 10^{-8}$
$\text{BR}(\tau^- \to \mu^-e^+\mu^-)$	$<1.7 \times 10^{-8}$
$\text{BR}(\tau^- \to \mu^+e^-e^-)$	$<1.5 \times 10^{-8}$
$\text{BR}(\tau^- \to e^-\pi)$	$<8.0 \times 10^{-8}$
$\text{BR}(\tau^- \to e^-\eta)$	$<9.2 \times 10^{-8}$
$\text{BR}(\tau^- \to e^-\eta')$	$<1.6 \times 10^{-7}$
$\text{BR}(\tau^- \to \mu^-\pi)$	$<1.1 \times 10^{-7}$
$\text{BR}(\tau^- \to \mu^-\eta)$	$<6.5 \times 10^{-8}$
$\text{BR}(\tau^- \to \mu^-\eta')$	$<1.3 \times 10^{-7}$
$\text{CR}_{\mu\to e}(\text{Ti})$	$<4.3 \times 10^{-12}$
$\text{CR}_{\mu\to e}(\text{Pb})$	$<4.3 \times 10^{-11}$
$\text{CR}_{\mu\to e}(\text{Au})$	$<7.0 \times 10^{-13}$
$\text{BR}(Z^0 \to e^\pm\mu^\mp)$	$<7.5 \times 10^{-7}$
$\text{BR}(Z^0 \to e^\pm\tau^\mp)$	$<5.0 \times 10^{-6}$
$\text{BR}(Z^0 \to \mu^\pm\tau^\mp)$	$<6.5 \times 10^{-6}$
$\text{BR}(h \to \text{invisible})$	$<0.11 \times \cos(\alpha)^{-2}$

A. Free parameters

The scalar potential contains 12 parameters: four dimensionful and eight dimensionless. The two minimization conditions, together with the two scalar masses $m_{h_{1,2}}$, allow

TABLE III. Values of the selected input parameters for the numerical scan, with all mass parameters expressed in units of [GeV] and angles taken in degrees.

Parameter	Range
λ_2	$[10^{-2}, 1]$
λ_3	$[10^{-2}, 1]$
λ_4	$[10^{-2}, 1]$
λ_5	$[10^{-10}, 1]$
$\lambda_3^{\eta\sigma}$	$[10^{-2}, 1]$
$\lambda_3^{\mathrm{H}\sigma}$	$[10^{-7}, 10^{-5}]$
m_η^2	$[9 \times 10^4, 2.5 \times 10^7]$
v_σ	$[10^3, 10^4]$
κ_{11}	$[10^{-2}, 1]$
κ_{22}	$[10^{-2}, 1]$
κ_{33}	$[10^{-2}, 1]$
m_{ν_1}	$[10^{-32}, 10^{-12}]$

us to fix four of these parameters. We choose them to be $m_{\mathrm{H}}^2, m_\sigma^2, \lambda_1$, and λ_σ. Consequently, the remaining free scalar parameters are

$$\{\lambda_2, \lambda_3, \lambda_4, \lambda_5, \lambda_3^{\eta\sigma}, \lambda_3^{\mathrm{H}\sigma}, m_\eta^2, v_\sigma\}. \tag{14}$$

For the new fermion sector, we consider the $\kappa_{\beta\beta}$ couplings as free parameters. Finally, in order to implement the Casas-Ibarra parametrization, m_{ν_1} is varied freely, along with the mixing angles of the PMNS matrix and the mass-squared differences of the neutrino masses within the experimental 3σ limits [19,20], while the arbitrary angles in the orthogonal matrix $\mathcal{O}$, as well as the Majorana phases, are varied between 0 and 2π. All in all, the free parameters are varied within the ranges displayed in Table III. In our numerical analysis, boundedness-from-below and vacuum stability are enforced via copositivity constraints among the quartic couplings [79,80]. Additionally, we restrict these couplings to positive values to reduce the parameter space and improve the efficiency of the MCMC scan. This defines a representative and well-behaved region, without qualitatively affecting our conclusions, as allowing negative values (consistent with copositivity) would only enlarge the parameter space.

B. The numerical method

The analysis of the model follows Refs. [50,51,81], using a PYTHON-based Metropolis-Hastings [82] algorithm, allowing us to efficiently scan, through an iterative process, the viable parameter space of the model.

The individual likelihood associated with each constraint is computed as

$$\ln(\mathcal{L}_i) = -\frac{(\theta^i_{\mathrm{obs}} - \theta^i_{\mathrm{exp}})^2}{2\sigma_i^2}, \tag{15}$$

where θ^i_{obs} represents the value of a specific observable estimated at a point i, θ^i_{exp} is the associated experimental result, and σ_i is the corresponding uncertainty, based on the list in Table II, which includes experimental bounds on the SM Higgs boson mass, the Higgs to invisible branching ratio, and constraints from LFV measurements. The final likelihood is then estimated from the product of all the individual likelihoods, assuming that the constraints are not correlated. The estimation is performed using a step function smeared as a single-sided Gaussian with a width of 10% relative to the experimental data, using Eq. (15). In cases where the observed value θ^i_{obs} is below the upper limit, the likelihood is equal to 1.

Because of the mixing in the scalar sector, the SM Higgs signal strength gets modified by a factor of $\cos^2\alpha$. Hence, it follows that the condition $|\sin\alpha| \lesssim 0.3$ must be fulfilled for $m_{h_2} > m_{h_1}$ [83–85], from the most recent LHC results [86,87]. In addition, direct searches for additional Higgs bosons give stronger bounds on $\sin\alpha$ than the Higgs signal strength for 150 GeV $< m_{h_2} \lesssim 700$ GeV [85]. Models that do not satisfy these collider bounds are excluded from our sample, independently of their likelihood.

In addition, the presence of a massless Majoron in the spectrum gives rise to both astrophysical and cosmological constraints. From the astrophysical perspective, Majorons can be copiously produced in the cores of stellar objects such as red giants and white dwarfs, where their emission provides an additional channel for energy loss. To remain consistent with well-established astrophysical observations, the rate of Majoron emission must therefore be sufficiently suppressed, which requires the Majoron-lepton couplings to be very small. In the present analysis, however, these constraints are significantly relaxed since the Majoron-lepton interactions arise only at the one-loop level and are thus loop suppressed. The assessment of the impact of these constraints is beyond the scope of this study and will be left as a secondary analysis. Additionally, as this study considers a massless Majoron, its presence could potentially affect the effective number of neutrino species, $\mathrm{N_{eff}}$, prior to recombination. As noted in Refs. [53,54], these effects could be significantly reduced if $\lambda_3^{\mathrm{H}\sigma} \lesssim 10^{-5}$.

After selecting the points that satisfy all the conditions outlined in Table II, we compute the relic DM density. We then exclude points that exceed the experimental upper bound, specifically applying the 3σ constraint $\Omega h^2 < 0.12$ from the Planck Collaboration [88]. Points yielding relic density values below the experimental value are retained, as they remain physically viable in scenarios where the DM candidate constitutes only a fraction of the total abundance. The parameter space is further constrained by a suite of experimental bounds arising from direct [89–92] and indirect [93,94] searches for DM; bounds on the oblique parameters S, T, and U [1,95] ($S = -0.01 \pm 0.10$, $T = 0.03 \pm 0.12, U = 0.02 \pm 0.11$); and exclusion bounds from the LHC [96,97]. We analyze the impact of these

results on the model's parameter space by selecting the points that fall within the corresponding allowed regions.

Our numerical MCMC analysis focuses on a compressed mass spectrum scenario. This choice is motivated by phenomenological studies [97–105]. Specifically, we require $\Delta m = |m_{\eta_R} - M_{N_1}| < 30$ GeV (50 GeV). This requirement enhances the role of coannihilation processes in the early Universe. For small mass splittings, the nearly degenerate $\mathbb{Z}_2$-odd states remain thermally populated during freeze-out, and their self-annihilations contribute to the effective annihilation cross section. This applies to both dark matter scenarios considered in this work: For fermionic dark matter, scalar annihilation channels can dominate the effective cross section, while for scalar dark matter, coannihilations with other scalar states and fermion self-annihilations can be relevant [106]. As a result, the relic abundance can be either reduced or increased compared to scenarios where only dark matter self-annihilation is relevant.[3] The subset of parameter space consistent with all experimental limits is subsequently employed to perform a feasibility study of the detection prospects for each DM candidate at the LHC. The results of this comprehensive analysis are presented in Sec. IV.

C. Collider analysis setup

A direct implication of a compressed mass spectrum is the low momentum of SM leptons arising from the $\eta^{0(\pm)} \to N_i + \nu_j(\ell^{\pm})$ decays. The reconstruction, identification, and analysis of final states with low-momentum leptons can be challenging at the experimental level. At the LHC, production from $q\bar{q}$ fusion can give rise to signals with the potential to be probed through DY processes such as $p + p \to \eta_I + \eta_R \to \eta_I + \eta^{\pm} + W^{\mp} \to \eta_I + \ell^{\pm} + N_i + W^{\mp}$ and $p + p \to \eta^{\pm} + \eta^{\mp} \to N_i + \ell^{\pm} + N_i + \ell^{\mp}$, where $\ell^{\pm}$ represents a SM charged lepton. Figure 2 shows representative Feynman diagrams for the DY production of scalar (left) and fermionic (right) DM signal processes at the LHC.

Purely neutral final states can be probed through VBF signatures. Experimentally, VBF processes are characterized by final states with charged leptons or missing transverse energy (E_T^{miss}) in the detector's central region, accompanied by two energetic jets with a large pseudorapidity gap, $\Delta\eta(j_1, j_2) > 3.8$, and large dijet invariant mass,

$$m_{jj} \approx \sqrt{2 p_T^{j_1} p_T^{j_2} \cosh(\Delta\eta(j_1, j_2))} > 500 \text{ GeV}. \quad (16)$$

This type of topology has been extensively explored in phenomenological studies as a powerful tool for searching for new physics at the LHC [98–102], and it has also been employed in experimental searches [97,104,105]. Moreover, VBF has proven valuable in Higgs boson to invisible branching fraction studies and in probing challenging regions of parameter space, such as those associated with compressed mass spectra in SUSY searches [96,97,119,120]. In the context of scotogenic models, VBF processes are particularly relevant due to the presence of Higgs portal interactions and the coupling of the inert scalar doublet η to electroweak gauge bosons. These features may allow VBF to access regions that remain inaccessible via DY production mechanisms. However, no dedicated study has yet been conducted in this direction. In the case of the dynamical scotogenic model, VBF production of DM particles can proceed either via resonant Higgs production or through W-mediated processes. Figure 3 shows representative Feynman diagrams for the VBF production of scalar (left) and fermionic (right) DM signal processes at the LHC.

With the objective of producing DM particles under a parameter space compatible with both the observed DM relic density and different experimental constraints enumerated in Table II, we transfer the values of the couplings and masses obtained from the scans to a set of files compatible with MadGraph. For this part of the analysis, we consider scenarios with $\Delta m < (30, 50)$ GeV and for the specific values $m_{h_2} = (246, 500)$ GeV.

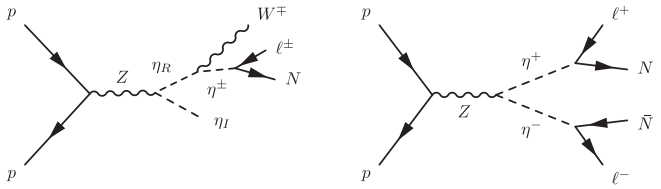


FIG. 2. Feynman diagrams associated with the production of DM via DY processes at the LHC. Left: sample topology for the production of the scalar DM candidate, η_I, along with a Majorana fermion and SM particles as final states. Right: sample topology for the production of the fermionic DM candidate, N_1, along with two SM leptons.

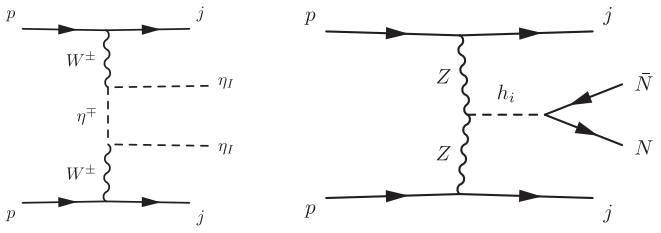


FIG. 3. Feynman diagrams illustrating the production of DM via VBF processes. The scalar DM channel is depicted on the left, while the fermionic channel is shown on the right.

[3]Compressed mass scenarios have been extensively explored in the context of supersymmetric models at the LHC, where they correspond to regions of parameter space that remain unconstrained by experimental searches [107–118].

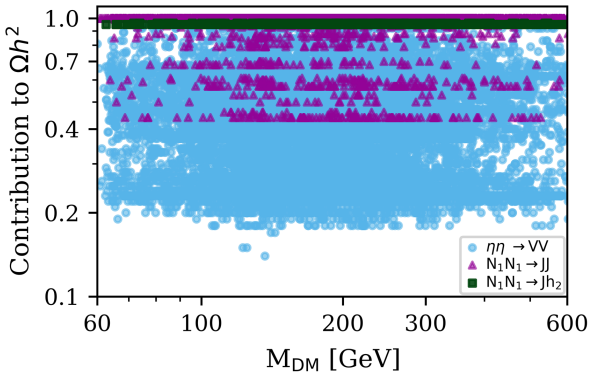


FIG. 4. Relative contribution of each process to the relic density projected on the DM mass when N_1 is the DM candidate and for $m_{h_2} = 246$ GeV and $\Delta m < 30$ GeV.

IV. PHENOMENOLOGICAL ANALYSIS

A. DM relic abundance

Following the methodology outlined in the previous section, we first analyze the DM relic density as a function of the DM candidate mass while incorporating all the constraints listed in Table II.

By imposing a compressed mass spectrum, the small mass splitting enhances the efficiency of coannihilation channels, thus causing them to play a significant role in determining the DM relic density. This behavior is illustrated in Figs. 4 and 5, where we have fixed $m_{h_2} = 246$ GeV and $\Delta m < 30$ GeV (similar results are found for $m_{h_2} = 500$ GeV).

For the case where N_1 is the DM candidate, the dominant annihilation channel is $N_1N_1 \to JJ$, while the $N_1N_1 \to Jh_2$ process is subdominant. In addition, annihilation processes of the inert doublet η into weak gauge bosons contribute significantly to the total DM annihilation rate, becoming, in some cases, the most dominant ones across the entire mass range of interest.

In the scenario where the pseudoscalar η_I is the DM candidate and no mass splitting is imposed, the standard inert-doublet behavior is recovered: For $m_{\eta_I} \lesssim 500$ GeV, the relic density is suppressed due to efficient gauge-mediated annihilations. When a compressed mass spectrum is enforced, however, N_1-induced processes may also become relevant. As illustrated in Fig. 5, fermionic channels involving N_1, such as $N_1N_1 \to JJ$ and Jh_2, can contribute significantly to the relic density. Furthermore, the $\eta\eta \to JJ$ process provides large contributions to the abundance in the resonance regions corresponding to $\frac{m_{h_1}}{2}$ and $\frac{m_{h_2}}{2}$, in contrast to the fermion DM scenario where the h_1 funnel region is suppressed by the small values of the $\lambda_3^{H\sigma}$ coupling.

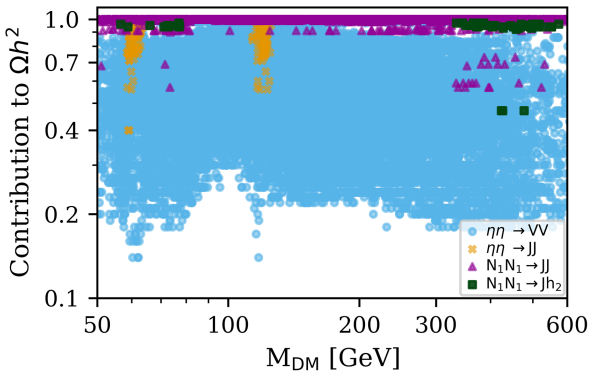


FIG. 5. Relative contribution of each process to the relic density projected on the DM mass when η_I is the DM candidate and for $m_{h_2} = 246$ GeV and $\Delta m < 30$ GeV.

B. DM direct and indirect detection

In both fermion and scalar scenarios, the direct detection of DM occurs through its elastic scattering off nuclei, mediated by the scalars h_1 and h_2 at tree level. Hence, sizable detection rates can arise in both scenarios. Since parameter-space points with a relic abundance below the observed value are also considered viable in this analysis, a rescaling factor ξ is introduced, defined as

$$\xi = \frac{\Omega^n_{\rm DM}}{\Omega_{\rm Planck}}, \tag{17}$$

where $\Omega_{\rm Planck}h^2 = 0.12$ is the central experimental value for the DM relic density reported by the Planck Collaboration [88], while $\Omega_{\rm DM}h^2$ is the relic density calculated for each point.

Figure 6 displays the rescaled spin-independent DM-nucleon scattering cross section, $\xi\sigma_{SI}$, as a function of the DM mass, for a fixed value of $m_{h_2} = 246$ GeV, noting that varying the value has a mild impact on the DM phenomenology. The solid lines correspond to the upper

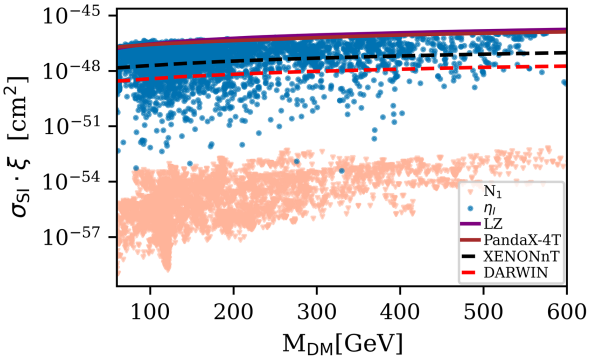


FIG. 6. Rescaled spin-independent cross section as a function of DM mass, for the two different DM candidates, N_1 (pink triangles) and η_I (purple circles). The solid lines represent the current upper limits reported by LZ and PandaX-4T experiments, while dashed lines represent the expected sensitivity from XENONnT and DARWIN. The points shown in the plot are consistent with the DM relic density constraint (within or below the current bound) and are within the compressed mass spectrum for $\Delta m < 30$ GeV and $\Delta m < 50$ GeV.

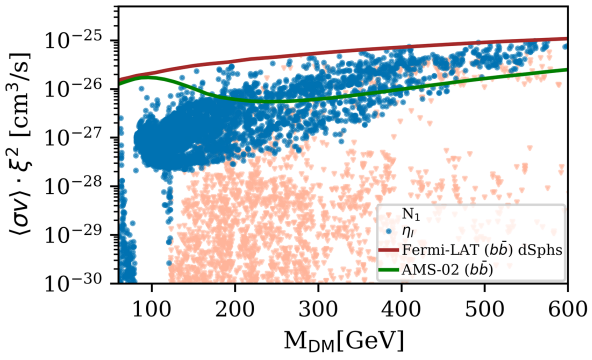


FIG. 7. Rescaled DM annihilation rates as a function of the DM mass, for the two DM candidates, N_1 (pink triangles) and η_I (purple circles), considering $m_{h_2} = 246$ GeV and both $\Delta m < 30$ GeV and $\Delta m < 50$ GeV. The solid lines represent the current limits imposed by the Fermi-LAT gamma ray data [93] and by the AMS-02 spectrometer [121]. The points shown are consistent with the relic density and direct detection upper bounds.

limits reported by the LZ [89] and PandaX-4T [90] Collaborations, while the dashed lines indicate the projected sensitivities for the XENONnT and DARWIN experiments [91,92]. Here, it is shown that the N_1-nucleon scattering cross sections are significantly suppressed to values below 10^{-53} cm^2. This suppression arises because the interaction proceeds exclusively through t-channel exchange of either h_1 or h_2. The corresponding vertex function depends explicitly on $\lambda_3^{H\sigma}$, which is assumed to satisfy $\lambda_3^{H\sigma} < 10^{-5}$. As a consequence, the resulting scattering cross sections are driven into the neutrino floor region. In contrast, when taking into account the projected sensitivities from future experiments such as XENONnT and DARWIN [91,92], large portions of the parameter space corresponding to the η_I DM candidate can be probed for masses ranging from 100 to 1000 GeV.

In addition to the direct detection, we also analyze the implications for the indirect detection of DM. The most relevant DM annihilation channels are $h_1h_1, h_2h_2, \mathrm{W}^{\pm}\mathrm{W}^{\mp}$. The corresponding rescaled rates are contrasted against the upper limits obtained from the Fermi-LAT data (in the $\mathrm{b\bar{b}}$ channel) using dSphs [93], assuming dominant $\mathrm{b\bar{b}}$ production, as shown in Fig. 7. Furthermore, the latest AMS-02 spectrometer results [121], which include the combined $\bar{p}$ and B/C ratios under the assumption of dominant $\mathrm{b\bar{b}}$ production, have also been incorporated. However, they were not employed as a constraint, owing to the strong model dependence of the associated propagation. Consequently, current indirect detection data do not impose any meaningful restrictions on the allowed parameter space of the model.

C. LHC signatures

1. Scalar DM scenario

To estimate the potential to probe the production of pseudoscalar states η_I at colliders via the DY mechanism, we calculate the cross-section values corresponding to a significance of 1.69σ. This threshold defines our expected exclusion at the 90% confidence level and is derived from the condition

$$\frac{S}{\sqrt{S + B + \delta_{\mathrm{Sys}}^2}} = 1.69, \tag{18}$$

where S is the expected number of signal events, B the total expected background, and the term δ_{Sys} corresponds to systematic uncertainties. Both S and B are proportional to the integrated luminosity $\mathcal{L}$ and their respective production cross sections. This simplified single-bin counting experiment provides a conservative estimate, as a full binned likelihood analysis exploiting the kinematic distributions and correlations would yield improved sensitivity[4] [123].

The estimated production cross-section values for the $\mathrm{pp} \to \eta_R\eta_I \to \mathrm{W}^{\pm}\eta^{\pm}\eta_I \to \mathrm{W}^{\pm}N_i\ell\eta_I$ process are obtained with MadGraph5_aMC, considering pp collisions at $\sqrt{s} = 13.6$ TeV for scenarios with $m_{h_2} = 246$ GeV, after including all the experimental constraints from Table II and a $\Delta m < 30$ GeV upper threshold. All points considered in the scan are consistent with the DM relic density, according to the estimates from Planck or values that fall below this threshold, as well as the current limits on DM-nucleon scattering from PandaX-4T and the upper bound on $\langle\sigma v\rangle$ from Fermi-LAT.

This analysis considers an optimistic scenario where background events constitute only 20% of the total expected yield. We include a flat 20% systematic uncertainty on the background rate and a 10% detector efficiency factor. The estimation of the observable signal region is performed for three LHC luminosity scenarios [124], $\mathcal{L} = \{137, 300, 3000\}$ fb^{-1}, which would be sensitive to cross-section values in the $[10^{-5}, 10^{-3}]$ pb range. However, our calculated cross sections for the viable parameter space fall in the $[10^{-18}, 10^{-10}]$ pb range, remaining several orders of magnitude below the required sensitivity. Consequently, we see that η_I production via DY processes is unlikely to be observable at the LHC in the foreseeable future.

As discussed in Sec. III C, the purely neutral final state can be probed via signatures from VBF processes at colliders. Specifically, we focus on producing signatures involving two pseudoscalar particles and two jets while explicitly excluding contributions from QCD processes and considering the processes illustrated in the left panel of Fig. 3. Similar final states have been studied in Ref. [97] within the context of SUSY models. We extrapolate their

[4]However, as commented in Ref. [122], this conservative single-bin approach comes at the cost of reduced sensitivity since extending the analysis to multiple bins can significantly strengthen the exclusion limits. Nevertheless, this approach is sufficient to establish the discovery potential and guide the phenomenological analysis.

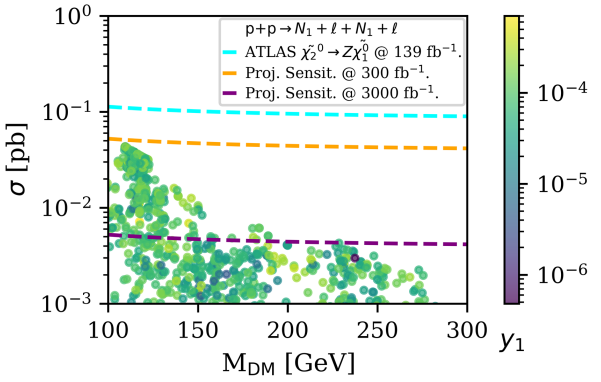


FIG. 8. Behavior of the $p + p \to N_i + \ell + N_i + \ell$ cross section as a function of the fermionic DM mass, for $\Delta m < 30$ GeV and $m_{h_2} = 246$ GeV. Dashed lines denote the experimental limits from ATLAS SUSY studies in compressed mass spectra models [96] (cyan), as well as expected sensitivities at $\mathcal{L} = 300$ fb^{-1} (orange) and $\mathcal{L} = 3000$ fb^{-1} (purple). The color map shows the different values for the $y_1 = \sqrt{|y_{N_1 e}|^2 + |y_{N_1 \mu}|^2 + |y_{N_1 \tau}|^2}$ Yukawa coupling.

results to our target mass ranges to estimate the detection feasibility for luminosity scenarios of 300 fb^{-1} and 3000 fb^{-1}, which imply sensitivity within the cross-section range $[10, 10^2]$ pb. However, we find that the production cross sections fall in the $[10^{-8}, 10^{-1}]$ pb range, just below the estimated limits.

2. Fermionic DM scenario

In fermionic DM production via DY mechanisms, the visible decay chain considered is $\eta^{\pm} \to N_1 + \ell$, as depicted in Fig. 2. This process generates two vertices that arise from the decay of each $\eta^{\pm}$, which introduces vertex functions proportional only to the Yukawa coupling y_{ij}. This contrasts with the scalar sector, where there is an additional dependence on λ_i arising from the η_R decay. Consequently, the cross section takes values from 10^{-2} pb down to 10^{-12} pb, higher than those in the scalar sector.

Figure 8 illustrates the behavior of the cross section as a function of the DM candidate in the fermionic sector. The requirement on $\Delta m < 30$ GeV yields expected final states that consist of soft leptons and invisible particles, similar to those studied in ATLAS SUSY analyses for compressed mass spectra in Ref. [96]. Therefore, we perform a recast of the ATLAS results, assuming the same experimental performance holds at higher luminosities. Our simulations are compared with the observed limits from Ref. [96] at $\mathcal{L} = 139$ fb^{-1}, and we extrapolate the expected sensitivities to $\mathcal{L} = 300$ fb^{-1} and $\mathcal{L} = 3000$ fb^{-1} under this assumption.

In contrast to the scalar sector, we observe that a portion is above the expected limits associated with $\mathcal{L} = 300$ fb^{-1} and $\mathcal{L} = 3000$ fb^{-1}. These results suggest that fermionic DM could be probed at the High-Luminosity LHC for mass ranges between 100 and 220 GeV, in searches targeting high $E_{\mathrm{T}}^{\mathrm{miss}}$ in association with low-momentum charged leptons.

For the purely neutral production of fermionic DM via VBF processes illustrated in the right panel of Fig. 3, we follow the same strategy used in the scalar sector, extrapolating the cross-section values obtained in Ref. [97] to our target mass ranges in order to estimate the detection feasibility for luminosity scenarios of 300 fb^{-1} and 3000 fb^{-1}. In this analysis, the extrapolated values fall in the same range as in the scalar VBF sector ($[10, 10^2]$ pb), whereas the production cross sections obtained take values in the $[10^{-8}, 10^{-3}]$ pb range, well below the aforementioned limits. The conjunction of DY and VBF results implies that the former mechanism could become a potential probe for fermionic DM, while VBF remains unsuitable for both DM particles, even at high-luminosity values at the LHC.

D. Scalar DM at FCC-hh

The gap between the experimental sensitivity and viable production cross sections could be closed at the Future Circular Collider (FCC) [125]. This facility promises center-of-mass collision energies approaching $\sqrt{s} \sim 100$ TeV, which would significantly enhance production rates, combined with ultrahigh luminosity $\mathcal{L} \sim 25$ ab^{-1} that could extend the probed parameter space.

Since the cross-section values obtained in the VBF analysis for the scalar sector lie close to the HL-LHC sensitivity prospects, we recalculate them at a center-of-mass energy of $\sqrt{s} = 100$ TeV, corresponding to the proposed center-of-mass energy for the hadronic ideation of FCC (FCC-hh) [125]. These calculations employ the NNPDF40_nlo_as_01190 parton distribution functions, which offer improved precision in the determination of proton structure [126]. Furthermore, we extrapolate the CMS limits and projected sensitivities from Ref. [97] to luminosities of 7 ab^{-1}, 15 ab^{-1}, and 25 ab^{-1}, values within the range expected from a 20–25 year operation of the FCC-hh [127].

Figure 9 shows the VBF production cross section as a function of the scalar DM mass, using the aforementioned $\sqrt{s} = 100$ TeV for the FCC-hh. Compared to the LHC results, the cross sections are notably larger due to phase space enhancement from the higher center-of-mass energy. However, the predicted cross sections fall slightly below the expected exclusion limit at $\mathcal{L} = 25$ ab^{-1}. Therefore, moderate improvements in integrated luminosity or analysis sensitivity could render these processes detectable for masses in the 150–200 GeV range. It is worth noting that such mass values are relatively low for FCC standards, which may exacerbate background and pileup levels and reduce the efficiency of analyses in this regime. While the FCC-hh will improve the accessible cross section compared

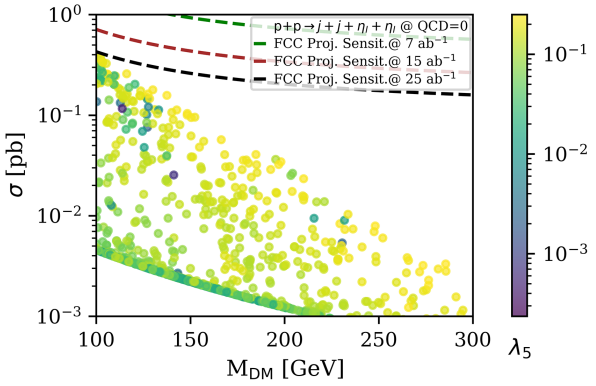


FIG. 9. Behavior of the $p + p \to j + j + \eta_I + \eta_I$ cross section as a function of the DM mass for $\Delta m < 50$ GeV. The green, brown, and black dashed lines are extrapolations of the SUSY VBF results from the CMS Collaboration [97] considering FCC luminosity scenarios of 7, 15, and 25 ab^{-1}, respectively.

to current experiments, the expected reach remains insufficient to firmly establish the detectability of DM for the mass range under consideration through VBF processes.

V. SUMMARY

We have conducted a DM and collider feasibility phenomenological study of the dynamical scotogenic model. This framework extends the SM by a $\mathbb{Z}_2$-even singlet scalar σ, a $\mathbb{Z}_2$-odd scalar doublet η, three Majorana fermions which are also odd under $\mathbb{Z}_2$, and a Goldstone boson (the Majoron) resulting from the $\mathrm{U}(1)_L$ symmetry breaking. In this setup, neutrino masses are generated radiatively at one-loop level through interactions involving the new $\mathbb{Z}_2$-odd states. The model naturally accommodates two viable DM candidates: the lightest Majorana fermion N_1 and the pseudoscalar η_I.

To assess the detectability of these DM candidates, we investigated both DY and VBF production mechanisms at hadron colliders. The analysis was carried out over the viable parameter space identified through a Markov chain Monte Carlo (MCMC) scan, incorporating all relevant experimental constraints, including the observed DM relic abundance, direct detection limits, collider bounds, and constraints from lepton-flavor-violating processes.

In the DY processes, we find that the scalar DM scenario consistently yields production cross sections below the projected experimental sensitivities for integrated luminosities of $\mathcal{L} = \{137, 300, 3000\}$ fb^{-1}. In contrast, the fermionic DM scenario exhibits cross sections that may be accessible at the High-Luminosity LHC, particularly in final states characterized by large missing transverse energy and soft leptons, for DM masses between 100 and 220 GeV. These sensitivity estimates are obtained by extrapolating existing ATLAS and CMS analyses performed in supersymmetric frameworks with similar final-state topologies.

For VBF production, we find that neither DM scenario leads to observable signals at the LHC. The predicted cross sections for scalar DM lie well below the expected sensitivity for luminosities between 300 fb^{-1} and 3000 fb^{-1} and DM masses between 100 GeV and 1 TeV.

Likewise, the cross-section values obtained for the fermionic scenario in the VBF channel remain far below the sensitivity estimates inferred from current ATLAS and CMS searches, even at the highest luminosities considered. These results stand in clear contrast to the DY case, where a limited but phenomenologically interesting region of parameter space remains accessible for fermionic DM.

All in all, our findings indicate that Drell-Yan production constitutes the most promising collider probe of fermionic DM in the dynamical scotogenic model, while VBF production is ineffective for testing either DM candidate, even at high-luminosity collider stages such as the HL-LHC or future facilities like the FCC.

ACKNOWLEDGMENTS

The authors express their sincere gratitude to Avelino Vicente and Valentina De Romeri for valuable discussions and insights regarding the model phenomenology and its implementation. A. F., C. R., M. S., and G. A. T. acknowledge the constant and enduring financial support received for this project from the Faculty of Science at Universidad de Los Andes (Bogotá, Colombia) through the Projects No. INV-2023-178-2999, No. INV-2023-175-2957, and No. INV-2024-199-3203. O. Z. acknowledges partial support from Sostenibilidad-UdeA, the UdeA/CODI Grants No. 2022-52380 and No. 2024-76476, and the Ministerio de Ciencias Grant CD 82315 CT ICETEX 2021-1080.

DATA AVAILABILITY

The datasets generated and analyzed during the current study are publicly available on Zenodo [128].

[1] S. Navas *et al.* (Particle Data Group), Phys. Rev. D **110**, 030001 (2024).
[2] P. W. Higgs, Phys. Rev. Lett. **13**, 508 (1964).
[3] F. Englert and R. Brout, Phys. Rev. Lett. **13**, 321 (1964).
[4] P. W. Higgs, Phys. Rev. Lett. **13**, 508 (1964).

[5] G. S. Guralnik, C. R. Hagen, and T. W. B. Kibble, Phys. Rev. Lett. **13**, 585 (1964).
[6] D. E. Morrissey and M. J. Ramsey-Musolf, New J. Phys. **14**, 125003 (2012).
[7] L. Canetti, M. Drewes, and M. Shaposhnikov, New J. Phys. **14**, 095012 (2012).
[8] S. Davidson, E. Nardi, and Y. Nir, Phys. Rep. **466**, 105 (2008).
[9] G. Bertone, D. Hooper, and J. Silk, Phys. Rep. **405**, 279 (2005).
[10] M. R. Buckley and A. H. G. Peter, Phys. Rep. **761**, 1 (2018).
[11] K. K. Boddy *et al.*, J. High Energy Astrophys. **35**, 112 (2022).
[12] Y. Fukuda *et al.* (Super-Kamiokande Collaboration), Phys. Rev. Lett. **81**, 1562 (1998).
[13] Q. R. Ahmad *et al.* (SNO Collaboration), Phys. Rev. Lett. **89**, 011301 (2002).
[14] P. J. E. Peebles, Astrophys. J. Lett. **263**, L1 (1982).
[15] G. R. Blumenthal, S. M. Faber, J. R. Primack, and M. J. Rees, Nature (London) **311**, 517 (1984).
[16] G. Steigman, B. Dasgupta, and J. F. Beacom, Phys. Rev. D **86**, 023506 (2012).
[17] L. Roszkowski, E. M. Sessolo, and S. Trojanowski, Rep. Prog. Phys. **81**, 066201 (2018).
[18] J. G. de Swart, G. Bertone, and J. van Dongen, Nat. Astron. **1**, 0059 (2017).
[19] I. Esteban, M. C. Gonzalez-Garcia, M. Maltoni, T. Schwetz, and A. Zhou, J. High Energy Phys. 09 (2020) 178.
[20] P. F. de Salas, D. V. Forero, S. Gariazzo, P. Martínez-Miravé, O. Mena, C. A. Ternes, M. Tórtola, and J. W. F. Valle, J. High Energy Phys. 02 (2021) 071.
[21] P. Minkowski, Phys. Lett. **67B**, 421 (1977).
[22] T. Yanagida, Prog. Theor. Phys. **64**, 1103 (1980).
[23] R. N. Mohapatra, Phys. Rev. Lett. **56**, 561 (1986).
[24] J. Schechter and J. W. F. Valle, Phys. Rev. D **22**, 2227 (1980).
[25] M. Gell-Mann, P. Ramond, and R. Slansky, in *Supergravity*, edited by D. Z. Freedman and P. van Nieuwenhuizen (North-Holland, 1979), pp. 315–321.
[26] F. Bonnet, M. Hirsch, T. Ota, and W. Winter, J. High Energy Phys. 07 (2012) 153.
[27] D. Restrepo, O. Zapata, and C. E. Yaguna, J. High Energy Phys. 11 (2013) 011.
[28] S. S. C. Law and K. L. McDonald, J. High Energy Phys. 09 (2013) 092.
[29] Z.-j. Tao, Phys. Rev. D **54**, 5693 (1996).
[30] E. Ma, Phys. Rev. D **73**, 077301 (2006).
[31] M. Klasen, C. E. Yaguna, J. D. Ruiz-Alvarez, D. Restrepo, and O. Zapata, J. Cosmol. Astropart. Phys. 04 (2013) 044.
[32] A. Ibarra, C. E. Yaguna, and O. Zapata, Phys. Rev. D **93**, 035012 (2016).
[33] D. Aristizabal Sierra, J. Kubo, D. Restrepo, D. Suematsu, and O. Zapata, Phys. Rev. D **79**, 013011 (2009).
[34] A. Vicente and C. E. Yaguna, J. High Energy Phys. 02 (2015) 144.
[35] T. Toma and A. Vicente, J. High Energy Phys. 01 (2014) 160.
[36] S. Fraser, E. Ma, and O. Popov, Phys. Lett. B **737**, 280 (2014).
[37] S. Baumholzer, V. Brdar, P. Schwaller, and A. Segner, J. High Energy Phys. 09 (2020) 136.
[38] D. Restrepo, A. Rivera, M. Sánchez-Peláez, O. Zapata, and W. Tangarife, Phys. Rev. D **92**, 013005 (2015).
[39] E. Molinaro, C. E. Yaguna, and O. Zapata, J. Cosmol. Astropart. Phys. 07 (2014) 015.
[40] R. Longas, D. Portillo, D. Restrepo, and O. Zapata, J. High Energy Phys. 03 (2016) 162.
[41] M. Lindner, M. Platscher, C. E. Yaguna, and A. Merle, Phys. Rev. D **94**, 115027 (2016).
[42] P. Rocha-Moran and A. Vicente, J. High Energy Phys. 07 (2016) 078.
[43] A. Ahriche, A. Jueid, and S. Nasri, Phys. Rev. D **97**, 095012 (2018).
[44] A. Betancur, R. Longas, and O. Zapata, Phys. Rev. D **96**, 035011 (2017).
[45] S. Bhattacharya, N. Sahoo, and N. Sahu, Phys. Rev. D **96**, 035010 (2017).
[46] S. Bhattacharya, P. Ghosh, N. Sahoo, and N. Sahu, Front. Phys. **7**, 80 (2019).
[47] A. Ahriche, A. Arhrib, A. Jueid, S. Nasri, and A. de La Puente, Phys. Rev. D **101**, 035038 (2020).
[48] P. Konar, A. Mukherjee, A. K. Saha, and S. Show, Phys. Rev. D **102**, 015024 (2020).
[49] P. Escribano, M. Reig, and A. Vicente, J. High Energy Phys. 07 (2020) 097.
[50] M. Sarazin, J. Bernigaud, and B. Herrmann, J. High Energy Phys. 12 (2021) 116.
[51] U. de Noyers, M. Sarazin, and B. Herrmann, Eur. Phys. J. C **85**, 922 (2025).
[52] C. Bonilla, L. M. de la Vega, J. Lamprea, R. A. Lineros, and E. Peinado, New J. Phys. **22**, 033009 (2020).
[53] V. De Romeri, J. Nava, M. Puerta, and A. Vicente, Phys. Rev. D **107**, 095019 (2023).
[54] E. J. Chun, A. Roy, S. Mandal, and M. Mitra, J. High Energy Phys. 08 (2023) 130.
[55] R. N. Mohapatra and G. Senjanovic, Phys. Rev. Lett. **44**, 912 (1980).
[56] R. N. Mohapatra and G. Senjanovic, Phys. Rev. D **23**, 165 (1981).
[57] L. Singh, R. Srivastava, S. Verma, and S. Yadav, Phys. Rev. D **112**, 095014 (2025).
[58] V. M. Lozano, G. S. Garcia, and J. W. F. Valle, Phys. Rev. D **112**, 055007 (2025).
[59] P. A. C., J. Zamora-Saa, and A. R. Zerwekh, Eur. Phys. J. C **84**, 1278 (2024).
[60] F. von der Pahlen, G. Palacio, D. Restrepo, and O. Zapata, Phys. Rev. D **94**, 033005 (2016).
[61] I. M. Ávila, G. Cottin, and M. A. Díaz, J. Phys. G **49**, 065001 (2022).
[62] G. Aad *et al.* (ATLAS Collaboration and CMS Collaboration), Phys. Rev. Lett. **114**, 191803 (2015).
[63] P. Escribano, V. M. Lozano, and A. Vicente, Phys. Rev. D **108**, 115001 (2023).
[64] P. A. Zyla *et al.* (Particle Data Group), Prog. Theor. Exp. Phys. **2020**, 083C01 (2020).
[65] J. A. Casas and A. Ibarra, Nucl. Phys. **B618**, 171 (2001).
[66] F. Staub, Comput. Phys. Commun. **181**, 1077 (2010).
[67] F. Staub, Comput. Phys. Commun. **182**, 808 (2011).
[68] F. Staub, Comput. Phys. Commun. **184**, 1792 (2013).
[69] F. Staub, Comput. Phys. Commun. **185**, 1773 (2014).
[70] W. Porod, Comput. Phys. Commun. **153**, 275 (2003).

[71] W. Porod and F. Staub, Comput. Phys. Commun. **183**, 2458 (2012).
[72] F. Staub and W. Porod, Eur. Phys. J. C **77**, 338 (2017).
[73] G. Bélanger, F. Boudjema, A. Goudelis, A. Pukhov, and B. Zaldivar, Comput. Phys. Commun. **231**, 173 (2018).
[74] A. A. Markov, *Extension of the Limit Theorems of Probability Theory to a Sum of Variables Connected in a Chain*, reprinted in Appendix B of: R. Howard, *Dynamic Probabilistic Systems, volume 1: Markov Chains*, (John Wiley and Sons, New York, 1971).
[75] A. Alloul, N. D. Christensen, C. Degrande, C. Duhr, and B. Fuks, Comput. Phys. Commun. **185**, 2250 (2014).
[76] C. Degrande, C. Duhr, B. Fuks, D. Grellscheid, O. Mattelaer, and T. Reiter, Comput. Phys. Commun. **183**, 1201 (2012).
[77] J. Alwall, M. Herquet, F. Maltoni, O. Mattelaer, and T. Stelzer, J. High Energy Phys. 06 (2011) 128.
[78] F. Staub, Comput. Phys. Commun. **241**, 132 (2019).
[79] K. Kannike, Eur. Phys. J. C **72**, 2093 (2012).
[80] M. Kadastik, K. Kannike, and M. Raidal, Phys. Rev. D **80**, 085020 (2009); **81**, 029903(E) (2010).
[81] A. Alvarez, A. Banik, R. Cepedello, B. Herrmann, W. Porod, M. Sarazin, and M. Schnelke, J. High Energy Phys. 06 (2023) 163.
[82] N. Metropolis, A. W. Rosenbluth, M. N. Rosenbluth, A. H. Teller, and E. Teller, J. Chem. Phys. **21**, 1087 (1953).
[83] A. Falkowski, C. Gross, and O. Lebedev, J. High Energy Phys. 05 (2015) 057.
[84] G. Arcadi, A. Djouadi, and M. Raidal, Phys. Rep. **842**, 1 (2020).
[85] T. Ferber, A. Grohsjean, and F. Kahlhoefer, Prog. Part. Nucl. Phys. **136**, 104105 (2024).
[86] G. Aad *et al.* (ATLAS Collaboration), Nature (London) **607**, 52 (2022); **612**, E24(E) (2022).
[87] A. Tumasyan *et al.* (CMS Collaboration), Nature (London) **607**, 60 (2022); **623**, E4(E) (2023).
[88] Planck Collaboration, Astron. Astrophys. **641**, A6 (2020).
[89] L.-Z. Collaboration, J. Aalbers, D. S. Akerib, C. W. Akerlof, A. K. A. Musalhi *et al.*, Phys. Rev. Lett. **131**, 041001 (2023).
[90] Z. Bo *et al.*, Phys. Rev. Lett. **134**, 011805 (2025).
[91] E. Aprile *et al.*, Eur. Phys. J. C **84**, 784 (2024).
[92] J. Aalbers *et al.*, J. Cosmol. Astropart. Phys. 11 (2016) 017.
[93] M. Ackermann and others (Fermi-LAT Collaboration), Phys. Rev. Lett. **115**, 231301 (2015).
[94] W. B. Atwood *et al.*, Astrophys. J. **697**, 1071 (2009).
[95] M. E. Peskin and T. Takeuchi, Phys. Rev. D **46**, 381 (1992).
[96] G. Aad and B. Abbott *et al.*, Phys. Rev. D **101**, 052005 (2020).
[97] A. M. Sirunyan and A. Tumasyan *et al.*, J. High Energy Phys. 08 (2019) 150.
[98] B. Dutta, A. Gurrola, W. Johns, T. Kamon, P. Sheldon, and K. Sinha, Phys. Rev. D **87**, 035029 (2013).
[99] B. Dutta, W. Flanagan, A. Gurrola, W. Johns, T. Kamon, P. Sheldon, K. Sinha, K. Wang, and S. Wu, Phys. Rev. D **90**, 095022 (2014).
[100] A. G. Delannoy, B. Dutta, A. Gurrola, W. Johns, T. Kamon, E. Luiggi, A. Melo, P. Sheldon, K. Sinha, K. Wang, and S. Wu, Phys. Rev. Lett. **111**, 061801 (2013).
[101] B. Dutta, T. Ghosh, A. Gurrola, W. Johns, T. Kamon, P. Sheldon, K. Sinha, K. Wang, and S. Wu, Phys. Rev. D **91**, 055025 (2015).
[102] C. Natalia, F. Andrés, G. Alfredo, J. Will, S. Paul, and T. cheng, J. High Energy Phys. 11 (2022) 026.
[103] A. M. Sirunyan *et al.* (CMS Collaboration), Phys. Rev. Lett. **124**, 041803 (2020).
[104] V. Khachatryan *et al.* (CMS Collaboration), Phys. Rev. Lett. **118**, 021802 (2017).
[105] V. Khachatryan *et al.* (CMS Collaboration), J. High Energy Phys. 11 (2015) 189.
[106] S. Profumo and A. Provenza, J. Cosmol. Astropart. Phys. 12 (2006) 019.
[107] T. C. collaboration, J. High Energy Phys. 08 (2019) 150.
[108] N. Cardona, A. Flórez, A. Gurrola, W. Johns, P. Sheldon, and C. Tao, J. High Energy Phys. 11 (2022) 26.
[109] A. Florez, T. A. Garces, and J. D. Ruiz-Álvarez, Phys. Rev. D **107**, 075010 (2023).
[110] U. S. Qureshi, A. Gurrola, and A. Flórez, Eur. Phys. J. C **85**, 1208 (2025).
[111] S. Ashanujjaman and S. P. Maharathy, Phys. Rev. D **107**, 115026 (2023).
[112] D. Agin, B. Fuks, M. D. Goodsell, and T. Murphy, Eur. Phys. J. C **84**, 1218 (2024).
[113] B. Dutta, T. Ghosh, A. Horne, J. Kumar, S. Palmer, P. Sandick, M. Snedeker, P. Stengel, and J. W. Walker, Phys. Rev. D **109**, 075018 (2024).
[114] P. K. Das, S. Dey, S. Kundu, and S. K. Rai, J. High Energy Phys. 05 (2025) 027.
[115] A. Flórez, L. Bravo, A. Gurrola, C. Ávila, M. Segura, P. Sheldon, and W. Johns, Phys. Rev. D **94**, 073007 (2016).
[116] C. Avila, A. Flórez, A. Gurrola, D. Julson, and S. Starko, Phys. Dark Universe **27**, 100430 (2020).
[117] E. Ballabene, Search for electroweak production of supersymmetric particles in compressed mass spectra with the ATLAS detector at the LHC, Ph.D. thesis, Milan University, U. Milan (main) (2022).
[118] L. Rossini, Search for supersymmetry with a compressed mass spectrum using the ATLAS detector, Ph.D. thesis, Milan University (2019).
[119] G. Aad and T. Abajyan *et al.*, Phys. Lett. B **716**, 1 (2012).
[120] S. Chatrchyan and V. Khachatryan *et al.*, Phys. Lett. B **716**, 30 (2012).
[121] A. Reinert and M. W. Winkler, J. Cosmol. Astropart. Phys. 01 (2018) 055.
[122] M. J. Baker, J. Fuentes-Martín, G. Isidori, and M. König, Eur. Phys. J. C **79**, 334 (2019).
[123] A. Segura and A. C. Parra, arXiv:2411.00706.
[124] C. Henderson (CMS Collaboration), SciPost Phys. Proc. **8**, 111 (2022).
[125] A. Abada *et al.* (FCC Collaboration), Eur. Phys. J. Special Topics **228**, 755 (2019).
[126] R. D. Ball, S. Carrazza, J. Cruz-Martinez, L. D. Debbio, S. Forte, T. Giani, S. Iranipour, Z. Kassabov, J. I. Latorre, E. R. Nocera, R. L. Pearson, J. Rojo, R. Stegeman, C. Schwan, M. Ubiali, C. Voisey, and M. Wilson, Eur. Phys. J. C **82**, 428 (2022).
[127] F. Zimmermann, M. Benedikt, X. Buffat, and D. Schulte, in *7th International Particle Accelerator Conference* (2016), p. TUPMW037.
[128] G. Ardila Tafurth, C. A. Flórez, O. Zapata, M. SARAZIN, and C. F. Rodriguez Cruz, Datafiles for collider feasibility of dynamical scotogenic model (2025).